Real-Time Dynamics Modeling of Cryogenic Ball Bearings With Thermal Coupling

Pradeep K. Gupta
PKG Inc.,
Clifton Park, NY 12065
e-mail: guptap@pradeepkguptainc.com

Howard G. Gibson
NASA/MSFC,
Marshall Space Flight Center,
Huntsville, AL 35812
e-mail: howard.g.gibson@nasa.gov

Real-time dynamic modeling of cryogenic ball bearings, where the rotating inner race accelerates to the operating speed, is based on integration of classical differential equations of motion of bearing elements, when experimentally measured ball/race traction behavior is used to compute the imposed acceleration on the rolling elements. The dynamic performance simulation provides a realistic coupling between traction behavior in the ball-to-race contacts and dynamics of bearing element motion as the bearing goes through the transient speed variation. However, due to vastly different mechanical and thermal time scales, heat generation in the bearing is time-averaged over a relatively large thermal time-step to model temperature fields as a step change, while the bearing motion is simulated in real-time. The emphasis is on dynamic modeling with thermal coupling in a static sense. Under stable conditions, the step change in temperature field converges to operating value as the bearing approaches a dynamic steady-state condition, which demonstrates acceptable significance of the dynamic simulation with coupled thermal interactions. Both all steel and hybrid ball bearings for liquid oxygen (LOX) turbo pump applications are modeled. Bearing performance simulations are closely modeled over experimental time cycles in both transient and steady-state domains. Steady-state solutions are shown to be independent of initial conditions to demonstrate acceptable convergence of time domain integrations. Model predictions of heat transferred to circulating LOX is within the range of variation in experimental data. Parametric evaluation of bearing performance as a function of operating conditions demonstrate that while the ball/race contact stress is higher in a hybrid bearing, contact heat generation is significantly lower in comparison with that in the all steel bearings. [DOI: 10.1115/1.4047582]

Keywords: rolling bearing dynamics, heat generation in rolling bearing, cryogenic bearings, space shuttle turbo pump, SHABERTH, ADORE, rolling element bearings

Introduction

Rolling element bearings on the main shaft of low and high pressure turbo pumps, which supply the cryogenic propellant to the space shuttle main engine are critical elements of the entire propulsion system. Failure of these bearings generally leads to catastrophic results. Since the cryogenic fluid flows through the bearings, no external lubricant to enhance the tribological characteristics at the rolling element-to-race interface may be supplied to the bearing; it is essential that the bearings survive the relatively high traction at the rolling element-to-race interface during both the transient and steady-state domains of the duty cycle. While thermal interactions in oil lubricated rolling bearings in gas turbine engines are important to ensure acceptable material and lubricant behavior, realistic modeling of contact heat generation at the rolling element-to-race contacts in the current application is significant in maintaining the liquid state of the cryogenic fluid flowing through the turbo pump bearings. In addition, an estimate of bearing heat generation provides viable guidance for the required amount of sub-cooling for the cryogenic fluid. Thus, aside from modeling of bearing motion under adverse time-varying operating conditions, realistic coupling of the dynamic effects with thermal interactions in cryogenic bearings has substantial practical significance.

As discussed in a historical perspective presented by Gibson et al. [1] most of the pioneering development work related to rolling bearings for cryogenic applications was carried out at NASA Marshall Space Flight Center during 1980s and 1990s. The starting point was the development of a unique test rig to experimentally evaluate the performance of ball bearings in cryogenic environment. The objective, at the time, was to experimentally measure the performance parameters to further develop the available computer codes for bearing performance modeling, such as SHABERTH [2], SINDA[1], and ADORE [3]. Perhaps, the most significant outcome of the initial bearing test results was the successful demonstration of the benefits of using silicon nitride balls in terms of reduced wear and contact heat generation [4]. Subsequent testing of hybrid bearings has further proven the improved performance of hybrid bearings in cryogenic environment [5].

In terms of dynamic performance modeling, particularly when the bearing is subjected to rapid accelerations, the traction-slip behavior in the ball/race contact is a significant input [3]. The traction-slip relationship controls both the steady-state slip and frictional heat generation at the ball/race contacts. Also, possibility of ball skid and resulting wear is related to the traction-slip relationship. Based on a traction tester developed by Tevaarwerk [6], Chang et al. [7] have examined such a behavior in rolling–sliding contacts operating in liquid oxygen (LOX) environment. In addition to examining surface damage and investigating scuffing as a function of surface roughness, this work has also published traction data as a function of slide-to-roll ratio at different rolling velocities. Both all steel and hybrid contacts are tested. This data serves as a significant input to the current bearing modeling tools.

While the NASA test rig, commonly referred to as Bearing and Seals Material Tester (BSMT) for testing ball bearings in cryogenic environment is described by Gibson [4], Moore [8] has extensively documented the experimental data generated over a decade at the

Contributed by the Tribology Division of ASME for publication in the JOURNAL OF TRIBOLOGY. Manuscript received December 3, 2019; final manuscript received June 15, 2020; published online September 1, 2020. Assoc. Editor: Noel Brunetiere.

[1]https://www.mscsoftware.com

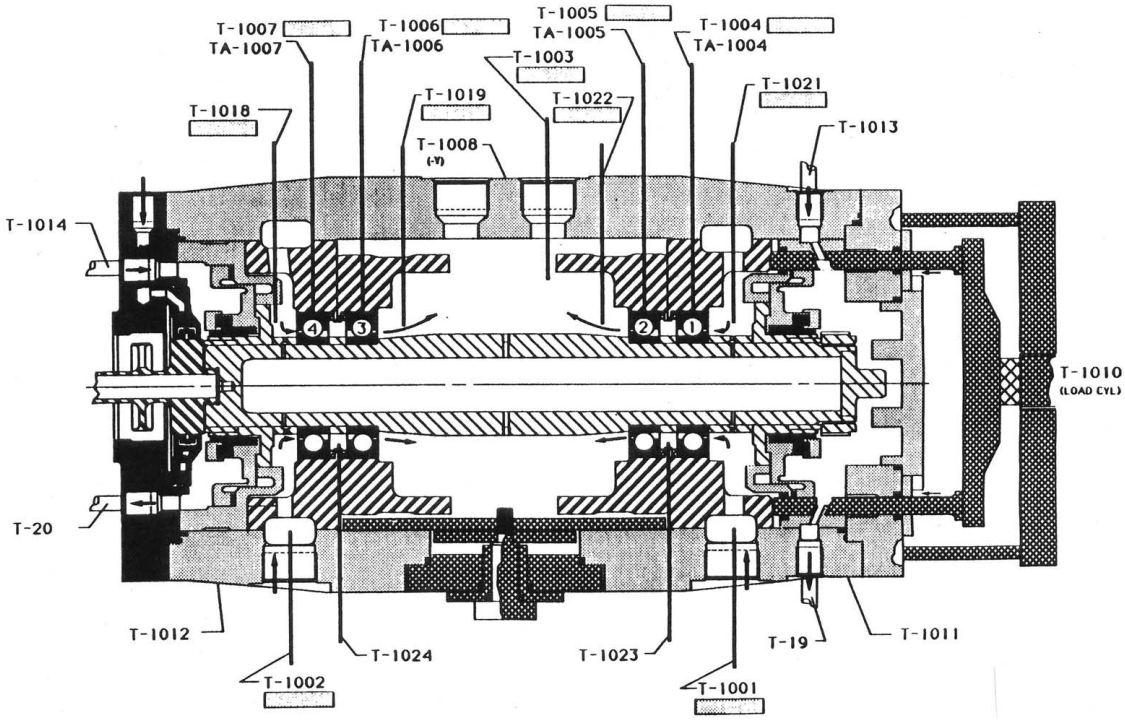

Fig. 1 Schematic of NASA BSMT

NASA laboratories. In addition, this work includes a thorough review of the modeling capabilities available at the time. SHABERTH [2] is interfaced with SINDA[2] to model overall thermal behavior from a systems perspective. In the quasi-static equilibrium formulation, such as the one used in SHABERTH [2], since the ball angular and orbital velocities are computed by kinematic considerations and empirical race control hypothesis, originally introduced by Jones [9], realistic modeling of slip in the ball/race contact is not possible. In addition, the transient variation in ball/race slip resulting from dynamic ball collision in the cage pockets cannot be modeled in a static equilibrium formulation. Hence, SHABERTH [2] offers limited capabilities in terms of modeling tribological behavior at the ball/cage and ball-to-race contacts, and the resulting contact heat generation and wear. Thus, under prescribed operating conditions, contact heat generation and cage dynamics is modeled by the dynamics code, ADORE [3], which is based on the integration of classical differential equations of motion. The applied force and moment vectors in the dynamic formulation include forces and moments from both the varying ball/race traction and transient cage pocket collisions. Although ADORE offers the capability to model imposed accelerations and resulting speed variations, it could not be effectively used, at the time, due to limitation in computing capabilities. Gibson et al. [10] presented the bearing testing work done at NASA Marshall Space Flight Center, emphasizing the fact that the bearings must support combined thrust and radial loads, and operate at high-speed with high wear resistance under no lubrication. The need for further development of modeling capabilities to meet these challenges is also emphasized.

Recent advances in both vector processing and several orders of magnitude increase in computing speed have made the compute-intensive dynamic performance modeling of rolling bearings, as structured in ADORE [3], possible within reasonable amount of computing effort. In addition, the advances in numerical procedures have further facilitated real-time dynamic modeling of rolling bearing. The objective of the current investigation is, therefore, to demonstrate such modeling capabilities and provide real-time simulations of bearing performance under both transient and steady-state conditions as applied in the NASA BSMT test rig. In addition, it is expected that the present investigation shall demonstrate the practical significance of current rolling bearing dynamic capabilities for any rolling bearing application in complex operating environment.

Experimental

Experimental bearing performance data is collected at the NASA Marshall Space Flight Center. Overview of the BSMT, the test bearings, and experimental procedures are outlined below.

Bearing and Seals Material Tester. A schematic of the BSMT is shown in Fig. 1. The tester houses four identical angular contact ball bearings and uses LOX as a coolant flowing through the bearings. All four bearings are subject to an identical thrust load and they operate at 30,000 rpm for a predetermined amount of time. There is no applied radial load in the system. Thus, mechanically all four test bearings are identically loaded.

The test rig consists of a number temperature and pressure sensors at various points in LOX flow path to monitor temperature and pressure at several points, as required in the performance simulations. In addition, several sensors are used for picking up any unusual activity, including cavitation, and activate automatic shutdown to ensure safe operation of the tests. The tester also has subcooling capability to ensure that after a rise in temperature, due to heat generation in the bearing, LOX stays in liquid state. For brevity, only the temperature sensors are shown in Fig. 1. A reference list of temperature sensors used in the present modeling effort is documented in Table 1. LOX inlet temperatures for bearings 1 and 4 are measured in the respective inlet ports, while the exit temperatures for these bearings are measured, respectively, by the sensors located between bearings 1 and 2 and between bearings 3 and 4. These temperatures are also used at inlet temperatures for bearings 2 and 3. Although there are two temperature sensors close to the exit from bearings 2 and 3 to measure the respective

[2]See Note 1.

Table 1 Reference list of temperature sensors used in the present investigation

Test bearing	LOX inlet	LOX exit
Bearing 1	T-1001	T-1023
Bearing 2	T-1023	T-1022
Bearing 3	T-1024	T-1019
Bearing 4	T-1002	T-1024

exit temperatures, the flow from these bearings is mixed at the exit. Therefore, a precise independence of these exit temperature measurements may not be guaranteed. Accuracy of measurement of the temperature sensors is within 1 °C of temperature measurement.

The main LOX supply is diverted to the two inlet ports, respectively, for test bearings 1 and 4, as schematically labeled in Fig. 1. The inlet pressure is measured at this point. Thus, the inlet pressure for bearings 1 and 4 is assumed to be the same. After passing through bearings 1 and 4, LOX flows through bearings 2 and 3, and the exit pressure is measured at that point. Thus, the exit pressure for bearings 2 and 3 is the same. There is no pressure measurement between bearings 1 and 2, and between 3 and 4. Assuming a linear pressure drop between the test bearings, the exit pressure at bearing 1 and inlet pressure at bearing 2 is assumed be average of inlet pressure at bearing 1 and exit pressure from bearing 2. Likewise, the exit pressure at bearing 4 and inlet pressure at bearing 3 is assumed to be average of inlet pressure at bearing 4 and exit pressure at bearing 3. Venturi orifice type flowmeter is used to measure the LOX low rate. A measurement error of less than 1% is expected for the total LOX flow. However, since the main LOX flow is diverted to the inlet ports of bearings 1 and 4, it may only be assumed that the flow diversion is equal. Likewise, it is assumed that the entire quantity of LOX entering the bearing chamber flows through the bearing and there is no leakage.

Assuming that a major fraction of heat generated in the bearings is extracted through the circulating LOX, the model output may be evaluated in terms of comparison of this quantity between model prediction and that computed from the experimentally measured temperatures and the expected flowrate. However, with the above discussion of the test rig architecture and instrumentation plan, the following expected discrepancies should be noted:

(1) When the temperature sensor has a prescribed accuracy of within 1 °C, and the measured temperature drop between exit and inlet is only 4 or 5 °C, calculation of the experimental value of heat extracted in LOX may be subject to 20–25% discrepancy.
(2) Likewise, the quantity of LOX flowing through the bearings is subject to uncertainties associated with the assumptions of equal quantity of LOX going through bearings 1 and 4 at the inlet and that the entire quantity of supplied LOX flows through the bearing without any leakage. This could also introduce significant uncertainty in the computation of experimental heat extracted in LOX.
(3) The mixing of LOX at exit from bearings 2 and 3 may affect both the measured exit temperatures and pressures for these test bearings.
(4) The assumption of linear pressure drop across the bearings affects the exit pressure at bearing 1, inlet pressure at bearing 2, exit pressure at bearing 4 and inlet pressure at bearing 3. Since LOX properties depend on both pressure and temperature these discrepancies affect both the LOX heat computed by the model and that computed for the experimental data.
(5) Aside from the above defined discrepancies, the experimental data and related inputs to the model may contain other unknown uncertainties related to adverse operating conditions, handling of LOX environment, system vibrations during the acceleration phases, and other variations in experimental conditions.

Since the four test bearings are geometrically identical, and they are identically loaded, the predicted behavior should be identical. With due recognition of the experimental discrepancies, however, it may not be possible to reliably differentiate between the operating conditions for each of test bearings. For the purpose of model evaluation, therefore, it may only be possible to input expected average operating conditions to the model and carryout validations of model predictions against the expected experimental average, which may be evaluated against the range of variation.

Liquid oxygen properties as function of pressure and temperature are readily available in the Reference Fluid Thermodynamic and Transport Properties (REFPROP) software, distributed by NIST [11]. In the present investigation, these properties are used for both the churning and drag effects and for the computation of heat extracted in the exiting LOX.

Test Bearings. Experimental data are generated for two sets of four bearings. The first set consists of all steel bearings, while the second set consists of hybrid bearings with silicon nitride balls. Geometrical overview of the test bearings is documented in Table 2.

Ball/Race Traction. Traction in the concentrated ball/race contact is perhaps the most significant parameter which controls the dynamic interactions in a ball bearing. In the current investigation, LOX simply flows through the bearing and there is no external lubricant at the ball-to-race contact. Tevaarwerk [6] developed a traction tester consisting of a concentrated rolling/sliding contact formed by a toroidal specimen pressed again a tire-shaped specimen mounted on a high-speed spindle; the contact load is applied in terms of simple dead weights and the contact is flooded with LOX. Using this tester, Chang et al. [7] investigated frictional interactions between steel versus steel and silicon nitride versus steel contacts in LOX environment. A series of tests are carried out with varying levels of surface finish at different rolling velocities, while the applied load is set at 400 N, which results in a contact stress of 2.2 GPa for the AISI 440C samples, and 2.9 GPa for the steel tire against silicon nitride toroid. Traction is measured as a function of slide-to-roll ratio and the onset of scuffing is investigated. In the current modeling effort, the data of interest is traction behavior, with relatively smooth surfaces, at the high rolling velocity. Figure 2 shows a typical data set for a 440C versus 440C rolling/sliding contact. At very low slide-to-roll ratios, the traction coefficient increases almost linearly until it reaches a maximum value of about 0.050 at a slide-to-roll ratio of about 0.0015, and then it stays relatively constant with increasing slide-to-roll ratio until the onset of scuffing at slide-to-roll ratios of 0.010.

A second series of tests are conducted with a silicon nitride toroidal specimen against 440C steel tire shaped specimen. As shown in Fig. 3, the traction coefficient again increases almost linearly with increasing slide-to-roll ratio but the maximum traction coefficient is only 0.025, which is reached again at a slide-to-roll ratio of

Table 2 Test bearing materials and geometries

Parameter	Bearing set 1	Bearing set 2
Ball material	440C	Silicon nitride
Race material	440C	CRB-7
Cage material	Armalon	Armalon
Number of balls	13	13
Bore (mm)	57.2567	57.2567
Ball diameter (mm)	12.70	12.70
Outer race curvature factor	0.550	0.530
Inner race curvature factor	0.530	0.530
Contact angle (deg)	22.33	25.84

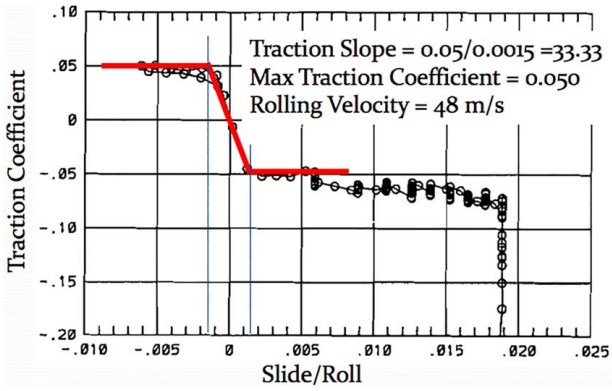

Fig. 2 440C versus 440C traction slip behavior at a contact stress of 2.2 GPa

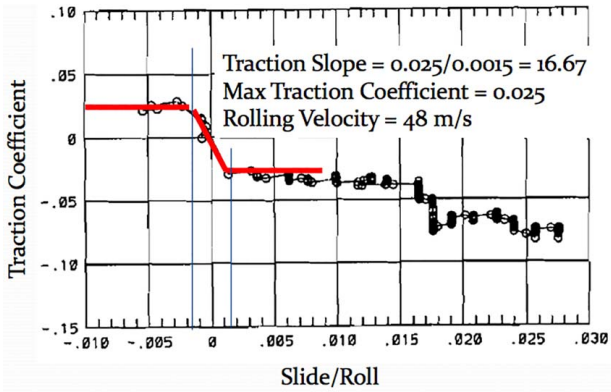

Fig. 3 Traction-slip behavior of a silicon nitride versus 440C steel contact in LOX environment at a contact stress of 2.9 GPa

0.0015 and the onset of scuffing moved further out to a higher slide-to-roll ratio. This reduction in traction and higher threshold for onset of scuffing are significant for the dynamic performance of hybrid bearing in LOX environment.

Cage Friction. The contacts at the ball/cage and cage/race interfaces are very lightly loaded but they are highly dynamic in nature. Unlike the ball/race contacts, these contacts are simple high-speed sliding contacts. Therefore, the frictional interactions are modeled by a simple friction coefficient. In the absence of any available data on friction coefficient for the armalon/440C and armalon/silicon nitride contacts, a constant friction coefficient of 0.050 is assumed in both 440C and hybrid bearings. Since the frictional dissipation in the cage contacts is insignificant in comparison with that at the ball/race contacts this assumption does not have a notable impact on overall heat generation. The significant role of cage interactions is in terms of ball/race slip introduced by the ball/cage and cage/race collisions during bearing operations. The resulting change in ball/race traction and contact heat generation is of course included in the dynamic simulations.

Test Procedure. Unlike the common bearing tests, which often run at constant speed for several hours, or sometimes several days, the test sequence for a typical test in the current investigation lasts for about 3–4 min. The sequence starts when an acceleration is applied on the inner race to bring the bearing to the operating speed of about 30,000 rpm in about 1 min. The bearing then runs for about 2–3 min as the operating temperatures, particularly the exit LOX temperature, stabilize. Figure 4 shows a typical test sequence where the recorded variation in temperatures, as obtained for a few of the temperature sensors, is plotted as a function of time.

While a large number of tests are carried out for both all steel and hybrid bearings, the number of tests selected for validation in the present investigation are tabulated in Tables 3 and 4, respectively, for the all steel and hybrid bearings. Model simulations are obtained in real-time over the entire duty cycle for each test sequence.

Modeling of Bearing Performance

As discussed earlier, bearing performance modeling in the present investigation is based on the bearing dynamics model ADORE [3]. The dynamic operating conditions, such as race acceleration to operating speed, are input into the dynamic equations of motion, which are integrated in real-time to obtain the bearing performance simulation as measured in the tester. In addition to the applied thrust load on the bearing, the equations of motion of bearing elements include the varying traction and centrifugal forces as the bearing race accelerates to operating speed. The generalized differential equations of motion of all balls and cage are integrated in time domain under the prescribed motion of the inner race. In order to couple the dynamic simulations with thermal interactions, a thermal averaging model is developed to obtain a thermal solution for steady-state bearing heat generation. The predicted heat generation is then validated against the experimental data to establish practical significance of the model. While the analytical foundation and related modeling details of the bearing dynamics code, ADORE, are available in open published literature [3], a brief analytical overview of the modeling steps used in the present investigation is presented below.

Input Race Acceleration. The transient part of the test sequence in Fig. 4 is modeled by imposing a constant angular acceleration on the inner race as the race speed increases from Ω_1 at time t_1 to Ω_2 at time t_2 as shown in Fig. 5

$$\dot{\Omega} = \frac{\Omega_2 - \Omega_1}{t_2 - t_1}, \quad t_1 \le t \le t_2 \tag{1a}$$

$$\dot{\Omega} = 0, \quad t < t_1 \quad \text{and} \quad t > t_2 \tag{1b}$$

In the current application, $t_1 = 0$, $t_2 = 60$ s, $\Omega_1 = 0$, and $\Omega_2 =$ operating speed.

Elements of Heat Generation in the Test Bearings. Thermal interactions in a rolling bearing very often control the overall performance of the bearing. The heat generated between interacting bearing elements travels through the bearing to the support system and in the process, alters the temperature field in the bearing. The changes in operating temperatures affect both the internal geometry and material properties, which alter interaction between bearing elements to modify the bearing load distribution, which in turn, feeds back to heat generation. Such an intricately coupled process continues until all solutions converge to steady-state conditions. In the event convergence cannot be reached, the bearing experiences a thermal instability and failure is eminent. Thus, realistic thermal modeling is a key element in the development of bearing performance simulation models. For cryogenic bearing in a turbo pump, where the cryogenic fluid flows through the bearing, heat generation is particularly important to ensure that the fluid does not vaporize and obstruct the flow. In other words, a realistic estimate of heat generation provides guidance for the required sub-cooling of the fluid for satisfactory operation.

In a rolling bearing in LOX environment, there are essentially two types of heat generation: frictional heat generated between all interacting bearing elements and LOX churning and drag losses

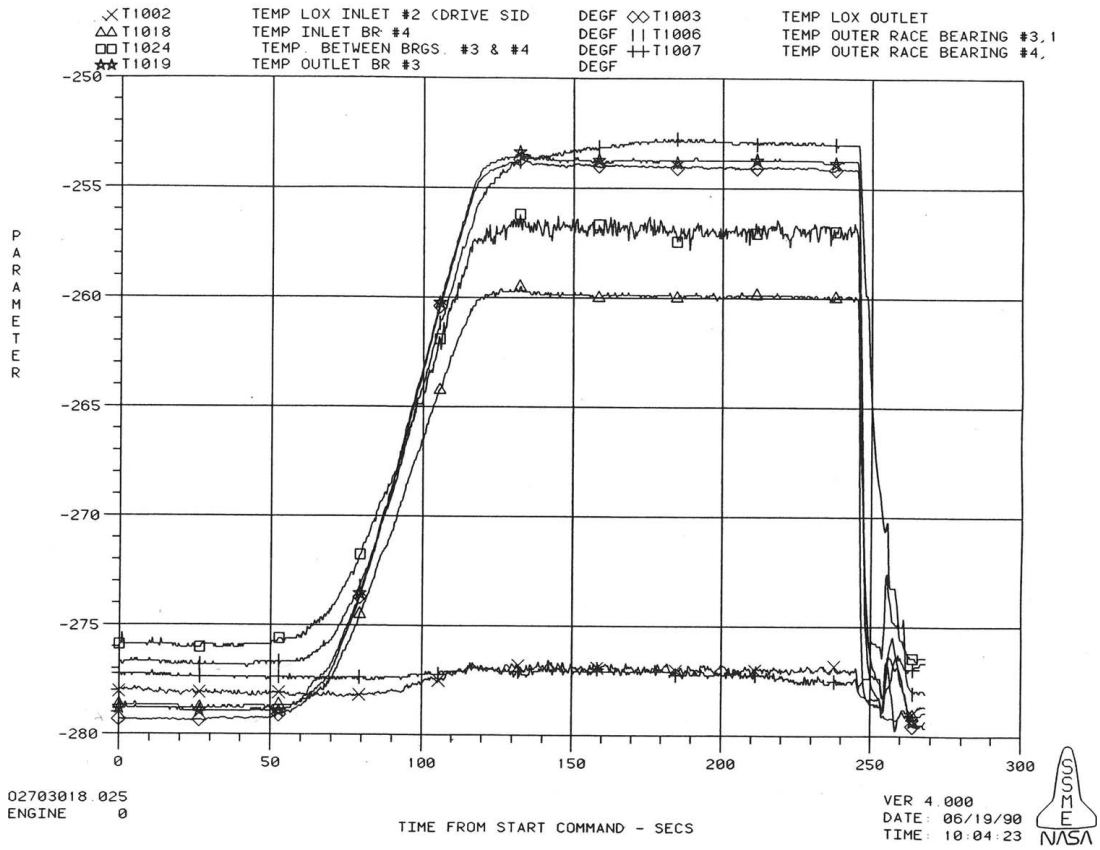

Fig. 4 A typical test sequence showing variation in temperature (°F) as a function of time

Table 3 Experimental data for 440C bearings

Test ID	310301	310402	310501	310703	310802	310901
Speed, kRPM	25	30	30	30	30	30
Thrust load, kN (lbf)	5.34 (1200)	6.67 (1500)	6.67 (1500)	6.67 (1500)	6.67 (1500)	6.67 (1500)
LOX flow rate, kgm/s (lbm/s)	2.09 (4.6)	2.09 (4.6)	2.09 (4.6)	2.09 (4.6)	2.09 (4.6)	2.09 (4.6)
Brg 1 LOX inlet temp, °K (°F)	118.2 (−247)	122.0 (−240)	120.4 (−243)	112.6 (−257)	119.8 (−244)	118.2 (−247)
Brg 1 LOX exit temp, °K (°F)	120.4 (−243)	124.8 (−235)	123.2 (−238)	120.9 (−242)	122.0 (−240)	120.4 (−243)
Brg 2 LOX exit temp, °K (°F)	122.0 (−240)	129.3 (−227)	128.2 (−229)	127.0 (−231)	126.5 (−232)	124.8 (−235)
Brg 4 LOX inlet temp, °K (°F)	118.2 (−247)	122.6 (−239)	120.9 (−242)	119.3 (−245)	119.3) (−245)	116.5 (−250)
Brg 4 LOX exit temp, °K (°F)	118.7 (−246)	123.7 (−237)	123.7 (−237)	120.4 (−243)	120.9 (−242)	118.7 (−246)
Brg 3 LOX exit temp, °K (°F)	123.2 (−238)	129.8 (−226)	128.2 (−229)	125.9 (−233)	127.0 (−231)	124.8 (−235)
Brg 1 and 4, LOX inlet pressure, MPa (lbf/in.^{2})	4.24 (615)	3.86 (560)	4.27 (620)	4.27 (620)	3.58 (520)	2.93 (425)
Brg 2 and 3, LOX exit pressure, MPa (lbf/in.^{2})	3.96 (575)	3.58 (520)	3.93 (570)	3.93 (570)	2.90 (420)	2.48 (360)

Note: All data values are rounded from experimental data sheets.

Table 4 Experimental data for hybrid bearings (440C races, silicon nitride balls)

Test ID	270301	270401	270501	270601	270705	270802
Speed, kRPM	25	26	28.25	30.30	30.20	29.90
Thrust load, kN (lbf)	6.67 (1500)	8.00 (1800)	8.00 (1800)	8.00 (1800)	8.00 (1800)	8.00 (1800)
LOX flow rate, kgm/s (lbm/s)	3.04 (6.7)	2.95 (6.5)	2.95 (6.5)	2.95 (6.5)	2.95 (6.5)	2.90 (6.4)
Brg 1 LOX inlet temp, °K (°F)	110.9 (−260)	118.2 (−247)	119.3 (−245)	119.9 (−244)	120.7 (−242)	123.7 (−237)
Brg 1 LOX exit temp, °K (°F)	111.5 (−259)	118.9 (−246)	122.0 (−240)	123.7 (−237)	123.7 (−237)	126.5 (−232)
Brg 2 LOX exit temp, °K (°F)	114.5 (−254)	121.9 (−240)	124.0 (−236)	125.6 (−233)	126.1 (−232)	129.3 (−227)
Brg 4 LOX inlet temp, °K (°F)	110.9 (−260)	117.2 (−249)	118.2 (−247)	119.0 (−245)	119.4 (−245)	122.6 (−239)
Brg 4 LOX exit temp, °K (°F)	112.6 (−257)	120.3 (−243)	121.4 (−241)	122.7 (−239)	122.7 (−239)	125.9 (−233)
Brg 3 LOX exit temp, °K (°F)	114.4 (−254)	121.5 (−241)	123.7 (−237)	125.7 (−233)	125.9 (−233)	128.7 (−228)
Brg 1 and 4, LOX inlet pressure, MPa (lbf/in.^{2})	3.10 (450)	3.06 (444)	3.05 (443)	3.07 (445)	3.07 (445)	3.07 (445)
Brg 2 and 3, LOX exit pressure, MPa (lbf/in.^{2})	2.90 (420)	2.83 (410)	2.83 (410)	2.83 (410)	2.83 (410)	2.83 (410)

Note: All data values are rounded from experimental data sheets.

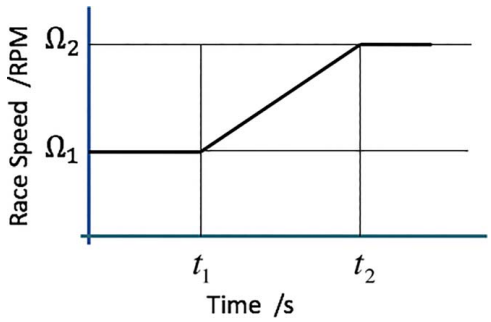

Fig. 5 Schematic of the model for inner race speed variation

as the rolling elements and cage travel through the fluid. While the rolling elements maintain contact with the races, support all the applied load, and roll over the races at relatively high-speed, purpose of the cage is to prevent contact between the rolling elements and avoid the very high-speed sliding between the rolling elements. However, introduction of the cage introduces frictional dissipation between the ball and cage, and also between the cage and race, when the cage is guided on one of the races. In addition, dynamic collisions of the balls in the cage pockets impose accelerations on the balls which modify ball/race slip, which in turn alters ball/race traction and the contact heat generation. All of these coupled interactions are included in the computed applied force and moment vectors in the differential equations of motion of bearing elements.

Rolling Element to Race Contacts. Rolling element to race contacts support all the applied load and the high-speed rotational motion between the outer and inner races. As a result of elastic deformation, the contact area between ball and race is elliptical in shape in ball bearings. Lubrication of these contacts has been known to be the most critical factor in controlling bearing performance. In conventional oil lubricated bearings, the ball and race surfaces are separated by a hydrodynamic lubricant film, and the coupled elastic and hydrodynamic, or elastohydrodynamic problem is solved to compute traction. Since the lubricant properties depend both on pressure and temperature, a thermal coupling in these solutions is also extremely important. In the current cryogenic application, however, there is no lubricant and the cryogenic fluid flows through the bearings. Due to extremely low viscosity, the hydrodynamic film generated by LOX is practically negligible, and therefore the contact is essentially metal-to-metal. The traction coefficient data discussed earlier in Figs. 2 and 3, perhaps, provide the most realistic modeling of the frictional behavior.

At any instant of time, the position of balls relative to the races defines the geometric interaction between the balls and races. This provides the applicable contact load and pressure at each contact. Likewise, the relative slip between the ball and races can be computed from the respective velocities. Since both the local pressure and sliding velocity vary from point-to-point in the contact area, the traction coefficient, and therefore the traction force is computed at each point in contact, per traction slip relation presented in Figs. 2 or 3. The corresponding heat generation is then a product of the traction force and sliding velocity. An integration of this product over the contact area provides the total heat generation in the contact

$$q_{ReR} = \int_A F' u \, dA \tag{2}$$

where q_{ReR} is total heat generation in the rolling element to race contact, F' is the traction force per unit area at any incremental area in the contact, u is the sliding velocity, and A is the contact area.

Frictional dissipation, as discussed previously, is the only source of heat generation at the ball-to-race contacts.

This computation is performed at both inner and outer races for each rolling element. All the heat generations are then summed to compute total heat generation in the rolling element-to-race contacts.

Rolling Element to Cage Contacts. As the ball accelerates in the cage pocket and ultimately collides with the pocket wall, a contact force is produced. While the collision velocities are output from integration of equations of motion, the contact force is determined by geometric interaction between the rolling element and cage, the applicable Hertzian point contact analysis and properties of the interacting materials. Details of the model has been documented by Gupta [3] and implemented in the dynamics code, ADORE. This force is highly dynamic in nature and quite small in magnitude in comparison with the load support forces at the rolling element to race contacts. Therefore, it may not affect the overall equilibrium of forces between the balls and races. However, the force is significant in defining motion of the cage and also slip in the ball/race contact. The time-step used in the integration of equations of motion is critical in realistic computation of this force. In ADORE once the geometric interaction indicates a contact, the applicable contact vibration frequency is computed and the step size is set to one fourth of the wavelength of this vibration. This permits a precise computation of the interacting force, the resulting ball acceleration and acceptable modeling of ball/cage contact cycle and its effect on ball/race interaction. The rotational motion of the ball also produces slip at the ball/cage interface, which leads to friction at the interface. In absence of any sliding friction data between the current materials a constant friction coefficient of 0.050, is assumed for these contacts, as discussed earlier. The resulting friction force is simply the product of computed normal force and friction coefficient. Finally, the heat generation in the contact is a product of friction force and sliding velocity

$$q_{ReC} = Fu \tag{3}$$

where q_{ReC} is the heat generation, F is the friction force, and u is the sliding velocity.

Again, heat generation at all the rolling element to cage contacts are summed to obtain the total heat generation in all cage contacts.

Cage to Race Contacts. When the cage is guided on the race, the nature of cage-to-race contact is similar to that between rolling element and cage; however, unlike the ball/cage contact, this is a line contact similar to the roller-to-race contact in a roller bearing. Again, the details of analysis of the cage/race interaction has been documented by Gupta [3] and implemented in the bearing dynamics code, ADORE. Similar to the ball-to-cage contact, the contact force is relatively low and the contact is subject to pure sliding. Therefore, the treatment is identical to that discussed above for ball-to-cage contacts. Again, similar to the ball-to-cage interface, the friction coefficient at this interface is assumed to be 0.050. Contact heat generation is then expressed by the relation similar to Eq. (3)

$$q_{CR} = Fu \tag{4}$$

where q_{CR} is the heat generation, F is the friction force, and u is the sliding velocity at the cage-to-race interface.

Generally, the cage has two guiding lands, one of each side of the rolling elements. Heat generations on both lands are summed to estimate the total cage-to-race contact heat generation.

Churning and Drag Losses. When the liquid oxygen flows through the bearing, the bearing cavity is essentially filled with LOX and both the balls and cage have to travel through LOX. This generates drag forces and churning moments, which not only affect bearing element motion but significantly add to bearing heat generation. Realistic modeling of these interactions is essential in modeling both the bearing element motion and overall heat generation. Primarily due to intricacies associated with internal geometry of a rolling bearing, a precise modeling of the lubricant flow

pattern is a very difficult task. A number of simplifying assumptions are necessary even in the most advanced computational fluid dynamics techniques. In view of these complications, modeling of drag forces, churning moments, and the resulting power losses is a highly empirical art. In the present investigation, the available models based on classical laminar and turbulent flows [12], originally developed by Rumbarger et al. [13], and implemented in ADORE [3], are used with an effective density and viscosity for the circulating fluid. Unlike the conventional bearings, since the entire bearing cavity is filled with LOX the applicable fluid density and viscosity are simply determined from the LOX properties at applicable pressure and temperature as available in the REFPROP software [11]. The key equations for computing the churning and drag effects are summarized in the Appendix for completeness.

Time-Averaging of Heat Generations. Although churning and drag losses are unaffected by subtle speed variations due to mechanical interactions between bearing elements, these dynamic variations do have a notable impact on contact heat generations between interacting bearing elements. Also, some of these heat generations, particularly the ones involving cage contacts, are highly dynamic in nature and typical heat generations, as obtained by integration of the differential equations of motion, appear as spikes over the base heat generation. While coupling of the overall dynamics of motion of bearing elements with these thermal interactions in terms of thermal transients with a very large time scale results in a computationally inefficient stiff system, static application of thermal interactions results in unrealistic high frequency temperature variations. Therefore, an approach based on time-averaging of the heat generation produced by dynamic interactions is developed. For a selected thermal step bounded by times t_{j-1} and t_j, the heat generation is averaged before applying a static thermal analysis

$$\bar{q}_j = \frac{1}{\Delta t}\int_{t_{j-1}}^{t_j} q(t)dt \tag{5}$$

where the thermal averaging step is defined as $\Delta t = t_j - t_{j-1}$.

An acceptable thermal step is selected by trial and error. Generally, a time interval corresponding to about ten revolutions of the bearing provides reasonable results. It must be noted that with such a thermal averaging process, the real-time simulation is only for the motion of bearing element and implementation of thermal interactions is essentially static and it results in a step change in the temperature field, which converges to a steady-state value as the dynamic solution reaches steady-state.

Since the initial conditions for dynamic simulation of bearing performance are generally selected arbitrarily, the initial transients in the dynamic interactions may be insignificant. Therefore, these transients may be skipped before heat generation averaging is initiated for thermal analysis. Under stable operation, the steady-state solutions do not depend on initial conditions, as will be demonstrated later.

Heat Transport and Operating Temperature Field. Once the heat generations at the various interfaces in the bearing are determined by the above time-averaging approach, a thermal analysis is required to compute the temperature field in the bearing. Due to obvious complexities associated with heat flow in the bearing, such an analysis is generally very complex and perhaps the best approach may be to carry out a finite element analysis. However, coupling such an analysis with the time-varying motion of bearing elements obtained by integrating the equations of motion introduces another level of complexity in the thermal analysis task. Thus, modeling of temperature field in the bearing as a result of bearing heat generation is greatly simplified in the present investigation. Following are the assumptions in the simplified model:

(1) Heat generated at rolling element to race contact travels via conduction to the rolling elements and races.
(2) All heat transferred to the races goes to the support system via conduction.
(3) Heat generated at all cage contacts is transferred via conduction to the cage and contacting elements.
(4) All heat transferred to the rolling elements and cage is transferred via convection to the circulating fluid.
(5) The heat generated due to churning and drag is added to the heat in the circulating fluid and travels out of the bearing.

The above simplification excludes the following, which may be significant in some application:

(1) Rigorous thermal interaction of the bearing with the application system, where heat generated by other system components may be input to the bearing.
(2) Heat convection from bearing surfaces other than that via circulating fluid.
(3) Heat conduction in the circulating fluid.
(4) Complex heat flow patterns in the bearing elements as often modeled by finite element analysis.
(5) Other specific application-dependent considerations.

The above more complicated aspects of thermal modeling require much more sophisticated finite element and/or finite difference modeling, which cannot be easily interfaced with the transient bearing dynamics model due to grossly different time scales as discussed above. Perhaps, more sophisticated approach in the future could be based on an independent computation of transient dynamic response and implementation of this response as a transfer function in the more complex thermal model.

Conductive Heat Transfer. All conduction type heat transfer is based on the simple conduction equation:

$$q = -kA\frac{dT}{dx} \tag{6}$$

where q is the heat flux, k is thermal conductivity, A is the effective area for heat flow, and dT/dx is the temperature gradient. For the ball-to-race contacts, when the two interacting surfaces are moving, the heat generated at the contact may be partitioned between the ball and race. When the interacting ball and race are denoted by subscripts 1 and 2, respectively, and the total heat generated in the contact is q, then the partitioned heat flux may be written as

$$q_1 = \gamma q \tag{7a}$$

$$q_2 = (1-\gamma)q \tag{7b}$$

where

$$\gamma = \frac{\sqrt{\rho_1 c_1 k_1 U_1}}{\sqrt{\rho_1 c_1 k_1 U_1} + \sqrt{\rho_2 c_2 k_2 U_2}} \tag{7c}$$

Thus, heat partition is based on applicable thermal properties of the ball and race materials. Treatment of the ball-cage and cage-race contacts is similar to the above except that the thermal properties of applicable materials are used.

Convective Heat Transfer. Convective heat transfer is modeled as

$$q = hA(T_o - T_\infty) \tag{8}$$

where T_0 is the surface temperature and T_∞ is temperature of the fluid at exit. The heat transfer coefficient, h, is estimated from available empirical correlations in the literature [14–16]. The correlations are generally expressed in terms of three dimensionless parameters, the Reynolds number, Prandtl number, and Nusselt

number, which are defined as follows:

$$\text{Reynolds number:} \quad \text{Re} = \frac{\rho V D}{\mu} \tag{9a}$$

$$\text{Prandtl number:} \quad \text{Pr} = \frac{\mu c_p}{k} \tag{9b}$$

$$\text{Nusselt number:} \quad \text{Nu} = \frac{hD}{k} \tag{9c}$$

Convective heat transfer for the ball surface is approximated by the available relationship for spherical bodies in liquid [16]

$$\text{Nu} = \text{Pr}^{0.30}\left[0.97 + 0.68\sqrt{\text{Re}}\right] \tag{10}$$

The Reynolds number, as applicable to the balls, is based on ball orbital velocity. Although the cage is a cylindrical element, most of the convection is controlled by fluid flow through the pockets, which is quite complex. Therefore, in the present investigation, the Nusselt number for the cage is set equal to that computed for the balls. In addition, the race surface temperature is set equal to that computed for the ball surface. With these simplifying assumptions, the temperature field in the bearing relative to an input reference temperature is completely defined.

It must be noted that the above relationships assume that the bearing element is completely submerged in the fluid, which is realistic in the current application since the entire bearing cavity is filled with LOX. Since there are several balls in the bearing, flow over one ball, in general, may affect the flow over the other adjacent balls. However, since the balls are almost completely contained in the cage pockets, the flow interaction between the balls may be minimum. Therefore, the independent treatment as modeled above may be reasonable.

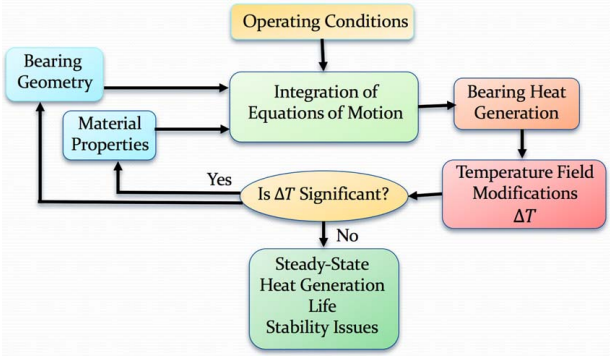

Fig. 6 Schematic representation of thermal interaction analysis in ADORE

Heat Flux in the Circulating Fluid. Finally, the total flux to circulating fluid is defined in terms of the inlet and exit temperatures is

$$q = mc_p(T_{exit} - T_{inlet}) \tag{11}$$

Since the heat transmitted to the races flows to the overall mounting system, computation of race temperature by simple radial conduction may be subject to substantial uncertainty. Therefore, an estimate of overall experimental bearing heat generation based on the measured temperature field is subject to significant uncertainty. However, as discussed earlier, since the fluid flowrate and input and exit temperatures are more precisely measurable, experimental estimate of the heat transferred to the circulating fluid, as defined above in Eq. (11), has the least uncertainty. It is, therefore, used to validate the model predictions.

Boundary Temperature for Computation of Temperature Field. As noted earlier, all thermal interactions are in terms of difference in temperature. Therefore, a boundary temperature, with reference to which, the temperature field in the bearing is computed, is needed. For the present investigation, the LOX inlet temperature, which is perhaps best defined, is taken as the reference temperature. The bearing temperature field leading to the LOX exit temperature may now be computed and the heat transferred to circulating LOX, as defined above in Eq. (11) may be validated against the experimental values.

Overall Model Implementation in ADORE. The above formulation of thermal interactions is implemented in the bearing dynamics code, ADORE [3], which integrates the equation of motion of bearing elements to provide a real-time dynamic simulation of bearing performance. The implementation is schematically described in Fig. 6. From the prescribed operating conditions, bearing geometry and material properties, which include frictional behavior, the equations of motion are integrated to obtain the bearing motion, interacting loads, moments, and heat generation. The computed heat generation is time-averaged, as discussed above, and then at appropriate time the thermal interaction analysis is carried out to calculate the temperature field in the bearing. If the temperature change is significant, then appropriate changes to bearing geometry, properties of bearing material, and circulating LOX are made and the transient dynamic analysis continues; the change in bearing geometry obviously alters all operating fits and clearances. Under stable conditions, the transient solutions and the temperature field converge to steady-state values. In the event, the temperatures do not stabilize to steady values; a thermal instability is indicated.

Results and Experimental Validation

For a typical test point, when the operating race speed is 30,000 rpm, the race speed variation as a function of time, as simulated in ADORE, with race acceleration described in Fig. 5, is shown in Fig. 7. From a static condition, the bearing speed increases

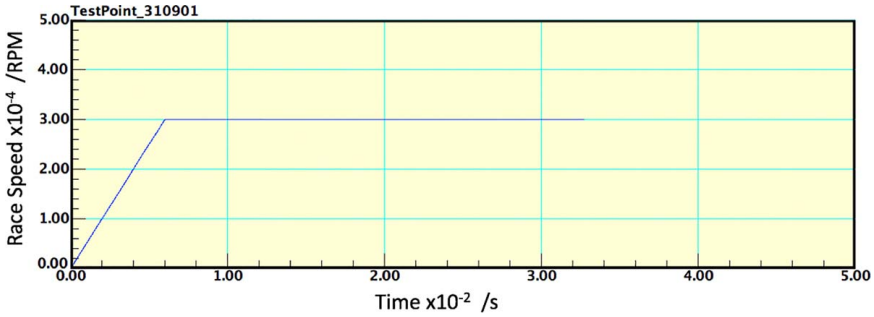

Fig. 7 Race speed variation as simulated in ADORE for a typical test point

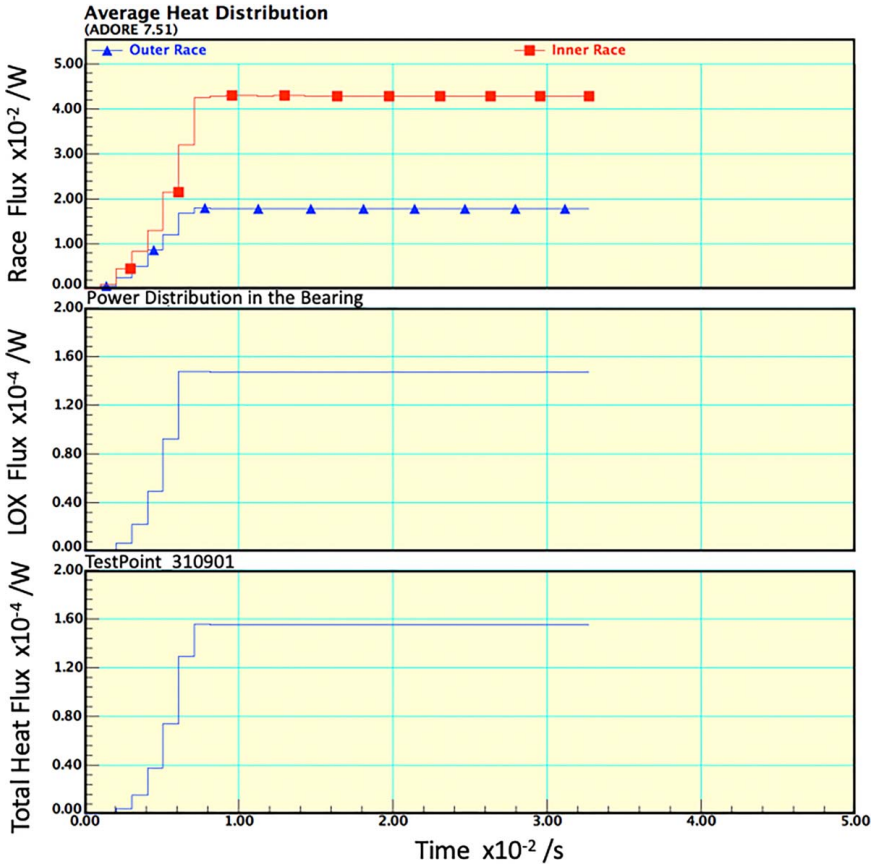

Fig. 8 Average power distribution between circulating LOX and bearing races

linearly, until it reaches the operating value of 30,000 rpm in 60 s. The acceleration is then cut off and the speed remains constant. Note that at 30,000 rpm centrifugal force on the balls is significant; the effect is, of course, included in the equations of motion of the balls. This effect is particularly important when comparing all steel versus hybrid bearings.

The distribution of time-averaged power between the circulating LOX and bearing races is shown in Fig. 8. Here, the computed heat generation is averaged over the thermal step; this contributes to the stepwise variation. For an inlet LOX temperature, the computed exit temperature from the thermal interaction analysis is shown in Fig. 9. Again, the stepwise increase is a result of the thermal averaging algorithm. Note that the magnitude of step change in temperature reduces as the solution converges to steady-state condition.

For the purpose of experimental validation, ADORE simulations for the test cases outlined in Tables 2 and 3, respectively, for the 440C and hybrid bearing are obtained. As discussed earlier, experimental validation is carried out by comparing the predicted heat transferred to LOX against that estimated, per Eq. (11), from the experimentally measured LOX temperatures and flowrate. Validations for the 440C bearings are shown in Fig. 10, which plots the experimental heat transferred to LOX against that predicted by ADORE. The plotted experimental value is average of the heat flux measured for the four test bearings. Although the applied load, speed, input LOX temperature, and flowrates are set to be identical for the four bearings in the tester, the LOX exit temperatures do show a variation. Corresponding to this temperature variation, the variation in heat flux is also plotted in Fig. 10. The notable difference in variation of heat generation over the four bearings between test points 310501 and 310703 could be correlated to a difference in input operating conditions. While the applied loads and speeds are of course identical, a closer look at Table 3 reveals that there is an 8 °K difference of LOX inlet temperature at bearing 1, while this difference is only about 1 °K at bearing 4. The sources for these variations have been discussed earlier when discussing the test rig under experimental procedures.

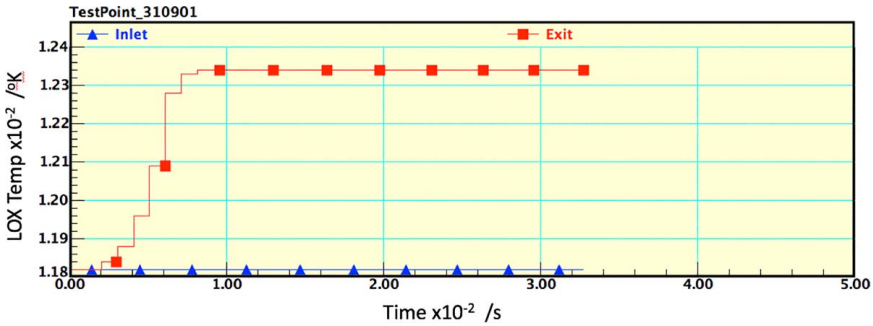

Fig. 9 LOX exit temperature as simulated by ADORE for a typical test point

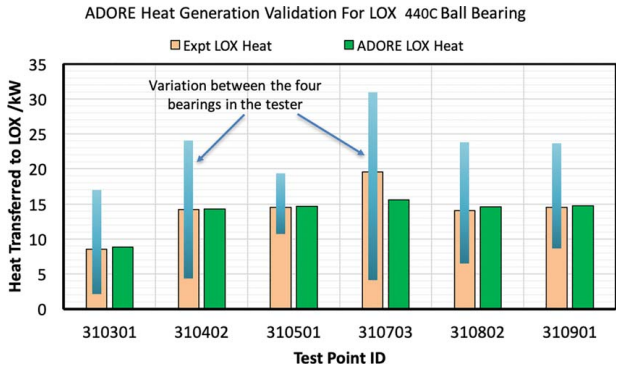

Fig. 10 Validation of bearing heat generation prediction against experimental data for the 440C bearings

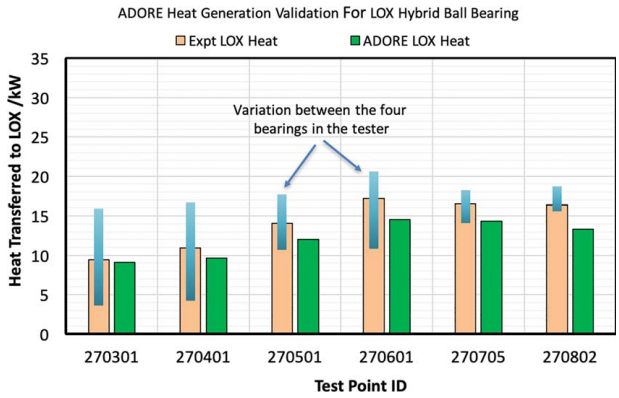

Fig. 11 Validation of bearing heat generation predictions against experimental data for the hybrid bearing with 440C races and silicon nitride balls

While the predicted heat generation is close to the average experimental value, the variation in experimental data is significant, as expected per experimental procedures discussed earlier.

A similar comparison between experimental measurement and model predictions for the hybrid bearings is shown in Fig. 11. In comparison with the 440C results shown in Fig. 10, ADORE predictions of heat generation for hybrid bearings are somewhat lower than the average of the experimental values. However, except for the last two test points, the predicted values are within the range of variation in the experimental data.

The experimental results and the corresponding model predictions in Figs. 10 and 11 are not expected to provide a comparison between hybrid and all steel bearing. In fact, the operating conditions, such as applied load and LOX flowrate are different in the two sets of bearings, as documented in Tables 2 and 3. Therefore, the datasets are not suitable for a one-to-one comparison, which is the subject of parametric evaluation later in this article.

Significance of Initial Conditions in Dynamic Modeling

Dynamic bearing performance simulations obtained by integration of differential equations of motion, as done in ADORE, require initial conditions to start the integration process. A question then comes up with regard to dependence of steady-state solution on initial conditions. Mathematically it may be proven that if the integration is convergent, as indicated by controlled truncation errors at each time-step, then the steady-state solution does not depend on the initial conditions; only the time required to reach steady state may depend on initial conditions. In other words, if the initial conditions are closer to the steady-state solution, then the steady-state condition may reach earlier. In order to prove this point for the present application, an alternate solution is obtained with the operating speed as initial condition for a typical test point.

Figure 12 shows two sets of initial conditions; a variable speed case, where the race starts from zero speed and accelerates to the operating speed of 30,000 rpm, and a constant speed case, where the operating speed is set 30,000 rpm upon start of the simulation.

ADORE is executed for the above two sets of initial conditions. The computed LOX exit temperature, as determined by the thermal averaging algorithm, with the two initial conditions are shown in Fig. 13, while the corresponding heat transferred to LOX is plotted in Fig. 14. Clearly, the steady-state solutions converge to same values under both sets of initial conditions.

The above two cases, with drastically different initial conditions, prove the independence of steady-state solution on initial conditions, which establishes the fact that the integration process used in the transient dynamic analysis is numerically convergent. This does not imply that transient analysis is not required for steady-state thermal modeling. In fact, since realistic modeling of slip between interacting bearing elements is a key element in contact heat generation, a transient dynamic analysis is necessary even at constant speed. In the coupled dynamics and static thermal analysis, as developed in the current investigation, it is the transient dynamics which provides the contact heat generation under prescribed tribological interaction between the interacting elements. Quasi-static bearing model, such as the systems model, SHABERTH, is only adequate when the contact heat generation and any tribological behavior between interacting bearing elements is ignored and bearing heat generation is defined only by the churning and drag effects which could be reasonably well computed by kinematic velocities determined in the quasi-static bearing analysis. In addition, since tribological interactions are the key elements of difference between all steel versus hybrid bearing, a transient dynamic

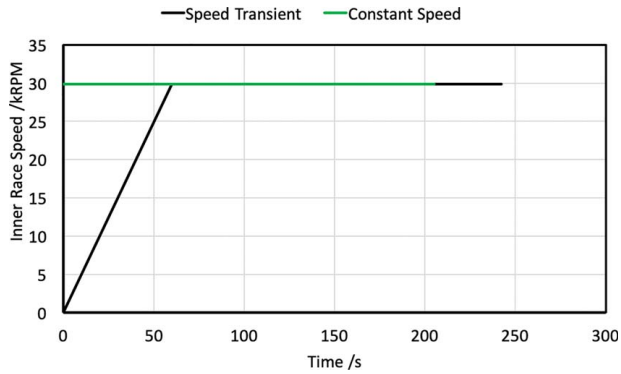

Fig. 12 Constant and variable race speed as initial condition in dynamic performance simulation

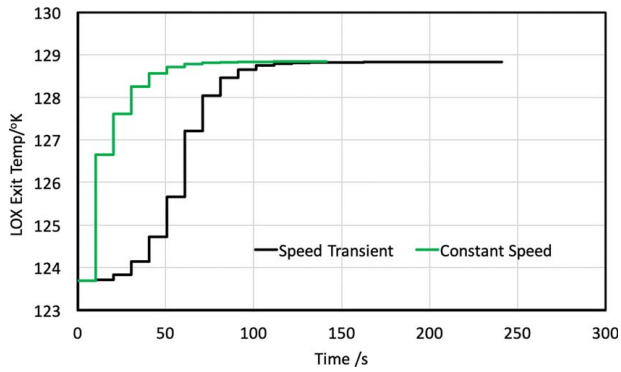

Fig. 13 Comparison of LOX exit temperature solutions with the two sets of initial race speed conditions for test point 270802

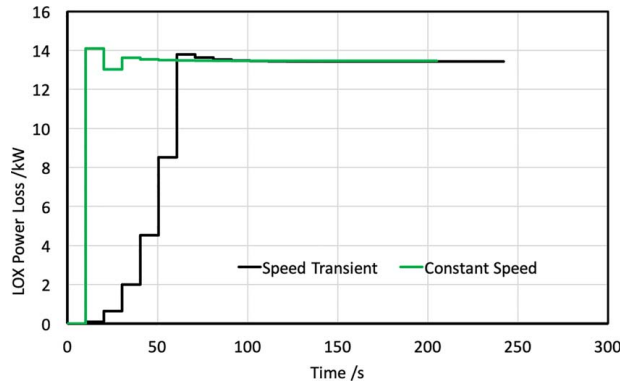

Fig. 14 Heat transferred to LOX with the two sets of initial conditions for test point 270802

analysis is required for such an evaluation. Normally, in transient dynamic analysis at constant speed, the simple quasi-static solution is used as initial condition. The above illustration demonstrating that the steady-state dynamic solution does not depend on initial conditions is significant in establishing the fact that the steady-state dynamic solution is not affected by any uncertainties in the initial conditions.

Parametric Evaluation of Hybrid Versus All Steel Bearings

Under a prescribed contact load, operating speed, and bearing geometry, simply due to higher modulus of elasticity of silicon nitride, the contact area is smaller and contact stress is higher in steel to silicon nitride contacts in comparison with all steel contacts. Although the higher contact stress leads to a lower fatigue life, the smaller contact area, depending on applicable traction coefficient, may lead to lower contact heat generation in hybrid bearings. However, for an angular contact ball bearing with a prescribed applied load and operating speed, since the centrifugal force on silicon nitride balls is lower than that on the steel balls, both the contact load and angles in hybrid and all steel bearings are different even with identical bearing geometries. Therefore, a complete bearing redesign is generally essential for optimum performance with prescribed bearing materials. In the present investigation, as documented in Table 1, there is a slight difference in bearing geometries for the steel and hybrid bearings; the outer race curvature factor is smaller for the hybrid bearings. This provides a slightly larger contact angle with the hybrid bearings. Also, as seen in Figs. 2 and 3, the hybrid contacts have a significantly lower traction coefficient; this greatly impacts the contact heat generation. While the contact loads and stresses, under prescribed elastic properties of interacting materials, may be well computed by equilibrium analysis, such as the one used in bearing systems code, SHABERTH [2], the ball angular and orbital velocities are computed by simple kinematics and empirical race control hypothesis, as introduced by Jones [9]. Therefore, the ball/race slip distribution, and the resulting traction and contact heat generation are not realistic in these models. Thus, a dynamic analysis, where the differential equations of motion of the bearing elements are integrated to obtain a steady-state motion and slip distribution in the ball/race contacts, is essential to better define the slip pattern and the resulting contact heat generation.

While the churning and drag effects depend only on the operating speed, and they are relatively unchanged between all steel and hybrid bearings, frictional dissipations depend on the applicable traction or friction between the interacting bearing elements, applied load and also the operating speed; these losses may, therefore, be greatly different between all steel and hybrid bearings. As discussed above, it is primarily this difference which necessitates a dynamic analysis for realistic evaluation of relative performance of hybrid versus all steel bearings. Thus, a number of parametric runs with the dynamics code ADORE [3] are undertaken as a function of applied load, at a typical operating speed of 30,000 rpm for both the all steel and hybrid bearings. Figure 15 plots the contact stresses, as determined by the applicable operating contact load and geometry. The difference between the contact stresses at the outer race between the steel and hybrid bearings is small; this is primarily a result of more conforming race curvature in the hybrid bearing, as documented in Table 1, and reduced centrifugal force with the silicon nitride balls. Contact stress at the inner race contact is significantly higher in the hybrid bearing since the inner race curvatures are identical in both steel and hybrid bearings. These observations suggest that for a given application the internal geometry of the bearing may be optimized for desired performance.

The total bearing power loss, including both the churning and drag losses and frictional dissipations, is plotted in Fig. 16 as a function of applied load at a race speed of 30,000 rpm. Note that while the total loss is lower in hybrid bearing, the load dependence of power loss (slope of the power loss to applied load relation) is slightly stronger in all steel bearing in comparison with that in the hybrid bearing. Since churning and drag losses are insensitive to the applied load, the load dependence is primarily a result of differences in frictional dissipations. Aside from difference in contact geometry and slip distribution in the ball/race contacts, the lower traction coefficient in the hybrid contact, as noticed by comparing Figs. 2 and 3, has a significant contribution to reduction in power loss in the hybrid bearing.

It may be emphasized that since the load dependence of bearing power loss or heat generation is a result of variation in contact heat generation, it cannot be realistically modeled in equilibrium models, such as the one used in SHABERTH [2], where the bearing heat generation is primarily based on churning and drag losses, which are insensitive to applied load, and relatively unchanged between all steel and hybrid bearings. Forster et al. [17,18] have also recently

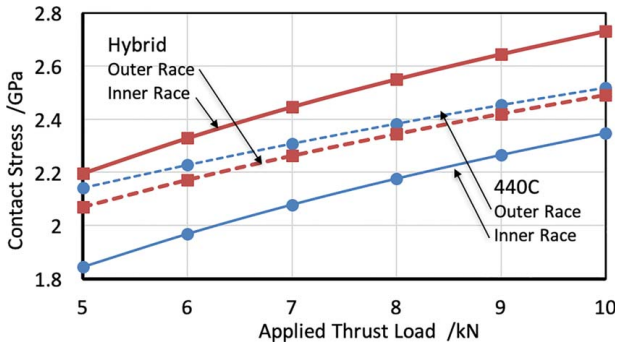

Fig. 15 Comparison on ball/race contact stresses in hybrid versus all steel bearing

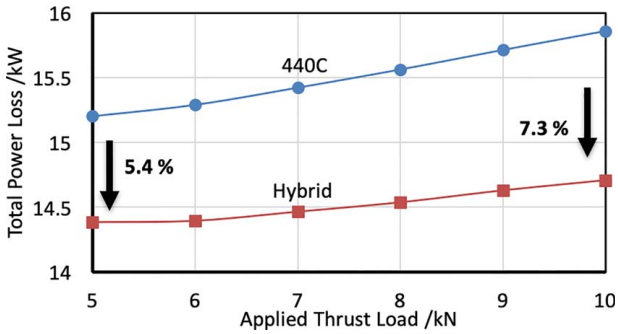

Fig. 16 Comparison of total power loss between the all steel and hybrid bearings as a function of applied thrust load at a race speed of 30,000 rpm

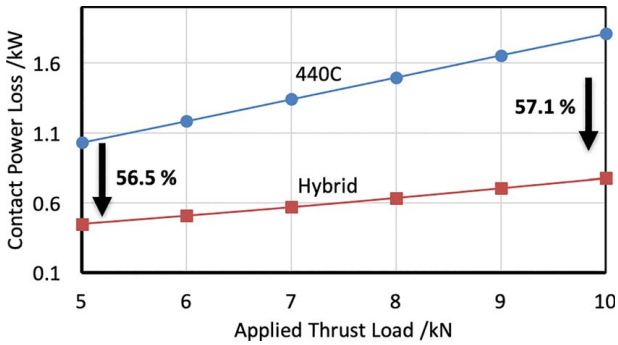

Fig. 17 Comparison of contact loss as a function of applied thrust load for the all steel and hybrid bearings at 30,000 rpm

pointed the load independence of SHABERTH [2] predictions of bearing heat generations.

While the churning and drag loss is unchanged between all steel and hybrid bearings, the heat generation in the ball/race contacts is greatly different. This is demonstrated in Fig. 17, where the variation in contact loss is plotted as a function of applied thrust load. Clearly, the contact loss in hybrid bearing is significantly lower than that in all steel bearing. Both the operating contact geometry and applicable traction coefficients contribute to this notable reduction in contact power loss in hybrid bearing. Furthermore, the relative reduction in contact power loss increases as the applied load increases. Such an observation demonstrates increasing improvement in thermal performance of hybrid bearing as the applied load increases. Again, the load dependence on these solutions is in line with those seen in Fig. 16.

In LOX environment, such a reduction in ball-to-race contact loss with hybrid bearings leads to improved tribological interactions at the ball/race interface and significantly improved overall bearing performance. Such a prediction is very much in line with the experimental observations reported by Gibson [4] and Moore et al. [5]. Based on such parametric evaluation of thermal performance, it is anticipated that the bearing performance simulation model developed in the present investigation may serve as a viable design tool for optimizing bearing design with prescribed materials and operating environment.

Summary

Classical differential equations of motion of bearing elements in a cryogenic ball bearing operating in LOX environment are integrated to obtain real-time dynamic simulation of bearing motion when the rotating race accelerates from zero to operating speed in the prescribed time under experimentally measured ball/race traction behavior. Thermal coupling of the bearing motion is accomplished by time-averaging the transient bearing heat generations over a substantially larger timestep before a thermal interaction analysis is applied to compute a step change in temperature field. Under stable operation, the temperature field converges to a steady-state value as the bearing reaches a dynamic steady-state. The resulting model thus eliminates the numerical and computational problems associated with greatly different mechanical and thermal time scales by providing a static coupling of thermal interactions with real-time dynamic motion of bearing elements to model steady-state behavior of the bearing. Model validation is presented by demonstrating that the predicted heat extracted in the circulating LOX is within the range of experimentally measured data for both all steel and hybrid ball bearing when the 440C balls are replaced by silicon nitride balls. Numerical stability of the integrating process is established by demonstrating that the steady-state solution is independent of initial condition. Parametric evaluation of steady-state ball/race contact heat generation show a significant reduction in heat generation with hybrid bearing.

Acknowledgment

The work reported in this article was funded by NASA Marshall Space Flight Center, Alabama under Purchase Order Numbers 80NSSC17P0282, 80NSSC18P1736, and 80NSSC19P0850 awarded to PKG Inc.

Nomenclature

c = specific heat (J/kg/°K)
f = friction factor
h = heat transfer coefficient (W/m^2/°K)
k = thermal conductivity (W/m/°K)
m = mass fluid flowrate (kg/s)
t = time (s)
u = slip velocity (m/s)
A = area (m^2)
D = diameter (m)
F = friction force (N)
M = moment (N · m)
T = temperature (°K)
U = velocity (m/s)
V = velocity (m/s)
F' = friction force per unit area (N/m^2)
C_D = drag coefficient
Nu = Nusselt number
Pr = Prandtl number
Re = Reynolds number
Ta = Taylors number
μ = viscosity (Pa · s)
ρ = density (kg/m^3)
ω = angular velocity (rad/s)
Ω = race speed (rpm)

Appendix: Churning and Drag Models

Drag forces on balls are generally estimated by empirical drag coefficients for spherical bodies:

$$F_D = C_D\left[\frac{1}{2}\rho V^2 \mathrm{A}\right] \tag{A1}$$

where C_D is the drag coefficient, the experimentally measured values of which are documented by Schlichtig [12], ρ is the effective density, V is the orbiting velocity, A is the frontal area, and F_D is the computed drag force. The frontal area on the rolling element is the area subjected to drag; this is simply the rolling element face area minus the area covered by the cage. The drag coefficient is generally expressed as a function of Reynolds number, Re,

$$\mathrm{Re} = \frac{\rho V D}{\mu} \tag{A2}$$

Here, D is a characteristic length, which is the rolling element diameter, and μ is the fluid viscosity.

Based on a wide range of experimental data, Schlichtig [12] has documented the drag coefficient as a function of Reynolds number for both spherical and cylindrical bodies. For completeness, the data for spherical bodies, as applicable to ball bearings, are replotted in Fig. 18. These data are interpolated to estimate applicable drag coefficient in the present investigation.

The resulting power loss due to this drag is simply the drag force multiplied by the orbital velocity.

Churning moments are significant on the cage as it turns through the fluid. Normally, there is a loss on both the cylindrical surface and end faces. An empirical formula for moment on the cylindrical surface is written as

$$M_c = \frac{1}{2} f \rho U^2 A r \tag{A3}$$

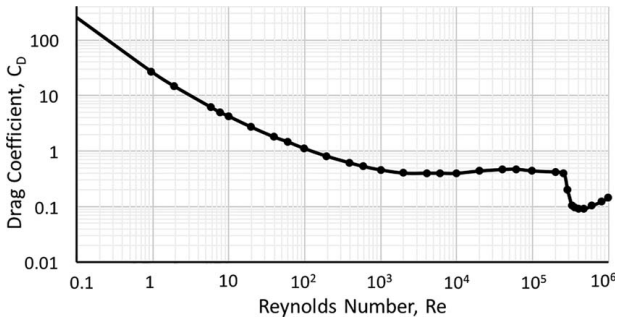

Fig. 18 Drag coefficient as a function of Reynolds number for spherical bodies

Here, ρ is the applicable density, A is the area, r is a reference radius from center of rotation, U is the mass average velocity of fluid, and the friction factor, f is defined as follows:

$$\text{Vortex turbulent flow:} \quad \frac{f}{f_L} = 1.3\left(\frac{\text{Ta}}{41}\right)^{0.539474}\Bigg|_{\text{Ta}>41} \tag{A4a}$$

$$\text{Couette turbulent flow:} \quad \frac{f}{f_L} = 3.0\left(\frac{\text{Re}}{2500}\right)^{0.85596}\Bigg|_{\text{Re}>2500} \tag{A4b}$$

$$\text{Laminar friction factor:} \quad f_L = \frac{16}{\text{Re}}\Bigg|_{\text{Re}<2500 \text{ or } \text{Ta}<41} \tag{A4c}$$

$$\text{Reynolds number:} \quad \text{Re} = \frac{\rho r \omega c}{\mu} \tag{A4d}$$

$$\text{Taylors number:} \quad \text{Ta} = \frac{\rho r \omega c}{\mu}\sqrt{\frac{c}{r}} \tag{A4e}$$

Generally, the reference radius, r, Is the radius of the rotating cylindrical surface; and c is the effective clearance between the rotating cylindrical surface and stationary housing.

For typical high-speed rolling bearings, the flow on cage surface is approximated as Couette turbulent.

For the end surfaces of the cage, the churning moment is written as

$$M_c = \frac{1}{2}\rho\omega^2 r^5 C_n \tag{A5a}$$

$$C_n = 3.87/\text{Re}^{0.50} \quad \text{for laminar flow} \quad \text{Re} < 300{,}000 \tag{A5b}$$

$$C_n = 0.146/\text{Re}^{0.20} \quad \text{for turbulent flow} \quad \text{Re} > 300{,}000 \tag{A5c}$$

$$\text{Re} = \frac{\rho r^2 \omega}{\mu} \quad \text{is the Reynolds number} \tag{A5d}$$

The effective radius, r, for the cage, which has the inner and outer radius, r_{in} and r_{out}, respectively, is approximated as

$$r^5 = r_{out}(r_{out}^4 - r_{in}^4) \quad \text{for laminar flow} \tag{A6a}$$

$$r^5 = r_{out}^{0.40}(r_{out}^{4.60} - r_{in}^{4.60}) \quad \text{for turbulent flow} \tag{A6b}$$

Although no explicit expressions for computing churning moment on the ball are available, the moment may be approximated by that occurring on a projected area normal to the ball angular velocity, which approximates it as a thin disk, with no cylindrical surface. Thus, Eqs. (A5*a*)–(A5*d*) may be used.

The churning loss is simply the product of computed churning moment and applicable angular velocity of rotation.

References

[1] Gibson, H., Thom, R., and Moore, C., 1998, "History of Space Shuttle Main Engine Turbopump Bearing Testing at the Marshall Space Flight Center," NASA Technical Reports Server (NTRS), Document ID: 19980193156.

[2] Crecelius, W. J., and Pirvics, J., 1976, "Computer Program Operating Manual on SHABERTH, A Computer Program for the Analysis of the Steady-State and Transient Thermal Performance of Shaft Bearing System," U.S. Air Force Technical Report AFAPL-TR-76-90.

[3] Gupta, P. K., 1984, *Advanced Dynamics of Rolling Elements*, Springer-Verlag, Berlin, Heidelberg, New York, Tokyo.

[4] Gibson, H. G., 1991, "An Evaluation of Bearings Operating in a Cryogenic Environment with Silicon Nitride Rolling Elements," NASA Technical Memorandoum, NASA TM-103524, January 1991.

[5] Moore, C., Gibson, H. G., and Thom, R., 1998, "Liquid Hydrogen Testing of Silicon Nitride Bearings for Use in High-Speed Turbomachinery," Proceedings of 32nd Aerospace Mechanisms Symposium, Complied by Walker, S. W. and Boesiger, E. A., May 13–15, pp. 197–212.

[6] Tevaarwerk, J. L., 1992, "Development of a Cryogenic Traction Tester," NASA Contract No. NAS8-38552, NASA/MSFC, Huntsville, AL.

[7] Chang, L., Hall, P. B., and Thom, R., 1998, "Scuffing Characteristics of High-Speed Rolling-Sliding Contacts Operating in Liquid Oxygen—Effects of Materials and Surface Roughness," STLE Tribol. Trans., **41**(1), pp. 87–95.

[8] Moore, J. D., 2000, "SSME Bearing and Seal Tester Data Compilation, Analysis and Reporting and Refinement of the Cryogenic Bearing Analysis Mathematical Model," SRS Technologies Technical Report prepared under NASA Contract NAS8-39379.

[9] Jones, A. B., 1960, "A General Theory of Elastically Constrained Ball and Roller Bearings Under Arbitrary Load and Speed Conditions," ASME J. Basic Eng., ASME Trans, Series D, **82**(2), pp. 309–320.

[10] Gibson, H. G., Robert, T., and Moore, C., 2010, "Space Shuttle Main Engine Turbopump Bearing Testing at Marshall Space Flight Center," NASA Technical Reports Server (NTRS), Document ID: 20100022057, Report #M10-0202, 57th JANNAF Joint Propulsion Meeting, May 3–7, Colorado Springs, CO.

[11] Lemmon, E. W., Bell, I. H., Huber, M. L., and McLinden, M. O., 2018, NIST Standard Reference Database 23: Reference Fluid Thermodynamic and Transport Properties-REFPROP, Version 10.0, National Institute of Standards and Technology, Standard Reference Data Program, Gaithersburg.

[12] Schlichtig, H., 1968, *Boundary Layer Theory*, McGraw-Hill, New York, pp. 15–19.

[13] Rumbarger, J. H., Filetti, E. G., and Gubernick, D., 1973, "Gas Turbine Engine Main Shaft Roller Bearing System Analysis," ASME J. Lubr. Technol., **95**(4), pp. 401–416.

[14] McAdams, W. H., 1954, *Heat Transmission*, McGraw-Hill, New York, pp. 265–268.

[15] Kreith, F., 1966, *Principals of Heat Transfer*, 2nd ed., International Text Book Co., Scranton, PA, pp. 410–415.

[16] Rohsenow, W. H., and Choi, H. Y., 1961, *Heat Mass and Momentum Transfer*, Prentice Hall, Englewood Cliffs, NJ, pp. 200–202.

[17] Forster, N. H., Svendsen, V. R., Givan, G. D., Thompson, K. L., Dao, N. H., and Nicholson, B. D., 2011, "Parametric Testing and Heat Generation Modeling of 133-mm Bore Ball Bearings: Part I—Results With Metal Rolling Elements," STLE Tribol. Trans., **54**(2), pp. 315–324.

[18] Forster, N. H., Svendsen, V. R., Givan, G. D., Thompson, K. L., Dao, N. H., and Nicholson, B. D., 2011, "Parametric Testing and Heat Generation Modeling of 133-mm Bore Ball Bearings: Part II—Results With Silicon Nitride Rolling Elements," STLE Tribol. Trans., **54**(2), pp. 325–331.